Detection of elemental mercury using a frequency-doubled diode laser with wavelength modulation spectroscopy

Xiutao Lou[1] · Lianjie Xu[1] · Yongkang Dong[2] · Tie Zhang[3] · Li Wan[4] · Sailing He[3]

Abstract

We demonstrate a new method for elemental mercury sensing by wavelength modulation spectroscopy (WMS) using a tunable ultraviolet laser generated through a process of second-harmonic generation (SHG). The WMS is implemented by fast modulating the injection current of the Fabry–Perot-type green diode laser equipped with a Littrow grating to increase the laser-mode power density. The technique of correlation spectroscopy is exploited to deal with the signal variations due to mode hops and guarantee the measurement accuracy. According to the performance evaluation, the SHG-WMS system exhibits a better sensitivity (0.15 μg/m^3 for 1-m pathlength with an integration time of 10 s) and a comparably high linearity ($R^2 = 0.9995$ within the range of 60 μg/m^2) compared with the direct absorption scheme. The employment of WMS significantly simplifies the data processing for extraction of small mercury absorption signals from the large and complex SHG light background, and, thus, give robust measurement results. High-harmonic ($4f$ and $6f$) detections are also carried out, showing a great potential for suppression of large residual amplitude modulation background. The proposed SHG-WMS system shows great promise for rapid and sensitive mercury sensing in industrial fields.

1 Introduction

Mercury is one of the most concerned pollutants due to its toxicity, especially to the nervous system and kidneys. Nearly, a third of annual mercury emissions to the atmosphere originate from anthropogenic sources [1]. The Minamata Convention on Mercury, a multilateral environmental treaty to protect human health from anthropogenic emissions, entered into force in 2017. In this treaty, coal-fired power plants and industrial boilers are listed as two major point sources of mercury emission [2]. To reduce the mercury emission from coal combustion, many mercury control technologies have correspondingly been developed [3]. It, therefore, calls for effective mercury monitoring techniques for the evaluation of mercury removal efficiency as well as the execution of corresponding regulations.

In coal-combustion exhaust, mercury exists in three forms: gaseous elemental mercury, gaseous oxidized mercury, and particle-bound mercury [4]. Detection of gaseous elemental mercury is of most importance as it is exceedingly difficult to remove due to its low reactivity and solubility [3]. In addition, the latter two forms of mercury can be converted to gaseous elemental mercury by a wet chemistry or thermal conversion unit. Currently, most of the elemental mercury analysis techniques are based on optical principles [5], mainly the spectrometry, using different light sources exploiting the strong 6^1S_0–6^3P_1 transition of mercury at 253.7 nm. The commonly used techniques include mercury-lamp-based cold vapor atomic absorption spectroscopy (CVAAS) [6], cold vapor atomic absorption spectroscopy (CVAFS) [7, 8], Zeeman-modulated atomic absorption spectroscopy (ZAAS) [9], and cavity-enhanced absorption spectroscopy (CEAS) [10]; xenon-lamp-based differential optical absorption spectroscopy (DOAS) [6]; laser-based cavity ring-down spectroscopy (CRDS) [11, 12],

✉ Xiutao Lou
  louxiutao@hit.edu.cn

  Yongkang Dong
  aldendong@gmail.com

[1] Department of Physics, Harbin Institute of Technology, Harbin 150001, China

[2] National Key Laboratory of Science and Technology on Tunable Laser, Harbin Institute of Technology, Harbin 150001, China

[3] Centre for Optical and Electromagnetic Research, National Engineering Research Center for Optical Instruments, Zhejiang University, Hangzhou 310058, China

[4] Suzhou Reliatek Environmental Technology Co., Ltd., Changshu 215558, China

light detection and ranging (LIDAR) [13, 14], and laser-induced fluorescence (LIF) [15]. The CVAAS and CVAFS are the two most widely used techniques in current commercial mercury continuous emission monitoring systems (CEMs) with high sensitivities at ng/m³ level (e.g., 10 ng/m³ with 180-s response time for the commercial CVAAS-based Mercury Instruments SM-4, and 2 ng/m³ with 300-s averaging time for the CVAFS-based Thermo Scientific 80i). However, these two techniques require sample preconcentration through gold amalgamation to remove interference species, which significantly degrades the responsibility of the system. Using the low-cost mercury-lamp-based CEAS, a high sensitivity of 66 ng/m³ has been achieved by greatly lengthening the absorption pathlength [10]. The ZAAS and DOAS have advantages of simplicity and high speed; their relatively low sensitivities at sub-µg/m³ level (e.g. 0.1 µg/m³ with 30-s response time for the commercial ZAAS-based Lumex Instruments RA-915J, and 0.5 µg/m³ for the DOAS-based Opsis 400Hg) can be improved using a long absorption pathlength. The CRDS, LIDAR, and LIF can achieve a high sensitivity down to sub-ng/m³ level (e.g., 0.35 ng/m³ for the CRDS with 300-s averaging time in [11], ~ 1 ng/m³ for the LIDAR with 1.5-s integration time in [14], and 0.015 ng/m³ for the LIF with 10-s acquisition time in [15]).

An alternative method for mercury detection is diode laser-based absorption spectroscopy. Diode lasers (DLs) have much longer life time (typically > 10,000 h) than mercury lamps (typically 2000 h), and they are much simpler and cheaper than the pulsed lasers. What is more important is their excellent tunability offering advantages of high speed and high specificity [16, 17]. For mercury detection, an ideal DL should have a single-mode emission around 253.7 nm with > 80-GHz tuning range. However, deep ultraviolet (UV) DLs are still not available and cannot be expected in the near future (considering the commercially available DLs at present are only down to 370 nm). Currently, the only approach to obtain a 253.7-nm UV laser is by frequency up-conversion through a nonlinear process such as sum frequency generation (SFG) [18–20], frequency-doubling (second-harmonic generation, SHG) [21, 22], and frequency quadrupling (two-stage SHG) [23, 24]. The frequency quadrupling approach can generate high-power UV laser radiation at mW level, but its configuration is relatively complex and the wavelength tuning range at even a moderate speed (> 10 Hz) is narrow (< 10 GHz). The SFG method was, for the first time, demonstrated by Alnis et al. in 2000 using a red DL with a newly available blue DL, but the achieved 35-GHz mode-hop-free tuning range was not adequate to acquire the whole mercury absorption feature [18]. In addition to direction absorption spectroscopy (DAS), they also demonstrated the possibility to employ wavelength modulation spectroscopy (WMS), but the measurement sensitivity was not improved due to the low power of UV laser at nW level. In 2007,

Anderson et al. developed an SFG-based mercury sensor with a continuous tuning range up to 100 GHz, achieving a sensitivity of 0.1 ppb (~ 0.9 µg/m³) for 10-s integration time, and successfully applied it to an actual coal-fired combustor [20]. They also tried implementing the WMS technique, which still brought no sensitivity improvement due to the low nW-level laser power. In 2015, the SHG approach was, for the first time, demonstrated by Almog et al. using a newly available 507-nm Fabry–Perot (FP)-type DL equipped with an external cavity configuration [21]. Although the generated UV laser could only be continuously tuned by a few GHz which limits its practical utility for mercury detection, the SHG presents evident advantages of simplicity and high robustness over other DL-based methods.

Recently, we have demonstrated an SHG-based method for mercury detection using a 507-nm FP-type multimode DL [22]. By introducing the technique multimode diode laser correlation spectroscopy (MDL-COSPEC) [25, 26], the frequent mode hops of the FP-DL were taken advantage of to provide an off-resonance baseline. In fact, the MDL-COSPEC technique was also successfully used in our earlier SFG-based mercury sensing systems [27]. Another technique termed multimode absorption spectroscopy (MUMAS) can also use MDL for gas detection [28], but its high requirement on the stability of the laser hampers its application to mercury detection using the newly available green FP-DLs.

In this paper, we report on an extension to our previous SHG-based mercury sensing works using wavelength modulation spectroscopy (WMS) [17, 29]. The FP-DL is equipped with a Littrow-type external cavity to concentrate the power into a few laser modes, while the WMS is implemented by fast injection-current modulation rather than the conventional external-cavity modulation. The laser outputs of intensity and spectrum are carefully characterized to optimize the system performance. To deal with the signal fluctuations due to mode hops and to guarantee the measurement accuracy, the MDL-COSPEC technique is employed. After optimization, the sensitivity and linearity performance of the SHG-WMS system are evaluated. Finally, potential schemes for further improving the measurement sensitivity are discussed.

2 Basic principle

2.1 Absorption spectrum of mercury

There exist seven stable isotopes of mercury (^{196}Hg, ^{198}Hg, ^{199}Hg, ^{200}Hg, ^{201}Hg, ^{202}Hg, and ^{204}Hg) [30]; as a result, the strong 6^1S_0–6^3P_1 transition of mercury at 253.7 nm presents a hyperfine structure due to isotope shifts and, for odd isotopes, nuclear spin splitting (the 6^3P_1 energy levels of ^{199}Hg

and ^{201}Hg split into two and three levels, respectively) [31]. Thus, the absorption spectrum of mercury at 253.7 nm actually contains ten transition components and each of their absorption cross sections can be expressed as [20]:

$$\sigma(\lambda) = \frac{A_{21}\lambda^2}{8\pi c} \cdot \frac{g_2}{g_1}\phi(\lambda)\text{NA}, \tag{1}$$

where A_{21} is the Einstein spontaneous emission coefficient, λ is the transition wavelength, c is the speed of light; g_1 and g_2 are the degeneracies of ground and excited states, respectively; $\phi(\lambda)$ is the absorption line shape modeled by Voigt profile involving both the Doppler and Lorentzian broadenings [20, 24]; NA is the natural abundance of the isotope. According to the transition formation provided in [20, 30–32], the absorption cross section of mercury is modeled and shown in Fig. 1. Clearly, the laser wavelength requires a tuning range > 0.2 nm (~ 110 GHz) to fully cover the absorption feature. This relatively high requirement is met in this work by using an FP-MDL and taking advantage of its frequent mode-hop behavior that can provide an off-resonance baseline and help to eliminate interferences from other gas species.

2.2 MDL-COSPEC with WMS

When using an MDL in the low-absorbance condition, the total effective absorption is simply an average of the absorptions by all individual modes weighted by the mode power. Correspondingly, the effective absorption cross section is written as follows [26]:

$$\sigma = \sum_n R_n \sigma_n, \tag{2}$$

where n denotes the nth mode of the MDL, and R denotes the intensity partition coefficient of the laser mode and obeys

Fig. 1 Absorption cross section of mercury at atmospheric pressure

$\sum_n R_n = 1$. Because of mode partition variations and even mode hops induced by mode competitions, the R and, thus, the σ always change irregularly with time. This problem can be perfectly resolved by the MDL-COSPEC technique [25, 26], in which a reference cell filled with a well-calibrated target gas is introduced to identify the target absorption signals in the sample path and retrieve the concentration of interest. In most cases, as detailed in Sect. 3.2, there often exist two major laser modes and only one of them is absorbed at each time; consequently, the maximum σ exploited in this work is around 1×10^{-14} cm^2/atom. Since the sample and reference laser beams originate from the same MDL source, the σ for them are identical and the absorption signals generated by the target gases in the two optical paths will always correlate in line shape. In contrast, disturbing signals coming from interfering gases or light intensity fluctuations, which are independent of the presence of the target gas, have totally different correlations and can, thus, be readily discriminated. The instrument function is mainly the Lorentzian profile of a laser longitudinal-mode spectrum. For a laser with external-cavity feedback, its typical linewidth is < 1 MHz, which is more than two orders of magnitude narrower than that of the mercury absorption profile (~ 25 GHz), and, therefore, has negligible effect on the σ.

In the limits of low absorbance and weak modulation, the second-harmonic component of the WMS signal is given by the following [17]:

$$A_2(\omega_C) = \frac{I_0 NL}{4}\delta\omega^2 \frac{d^2\sigma}{d\omega^2}\bigg|_{\omega=\omega_C}, \tag{3}$$

where ω_C is the center angular frequency of the laser, $\delta\omega$ is the modulation amplitude, I_0 is the initial laser intensity, N is the number density of the target gas, and L is the optical path length through the gas. By comparing the correlated sample and reference WMS-2f signals, the concentration of the sample gas can be retrieved according to the following:

$$N_S = N_R \frac{L_R}{L_S} \frac{A_{2S}(\omega_C)/I_{0S}}{A_{2R}(\omega_C)/I_{0R}}, \tag{4}$$

where the indices S and R denote the sample and the reference, respectively. In practical implementations, I_0 is obtained by a third-order polynomial baseline fitting to the detector DC signal, while the ratio between the intensity-normalized sample and reference WMS-2f signals is retrieved through a linear-regression procedure. Note that the concentration retrieval algorithm based on Eq. (4) is on the basis that the σ for the sample and the reference channels are identical. However, in practical applications, there may be differences in the isotopic composition of the sample and the reference mercury vapors, which could be up to ~ 0.5% [33]. The isotopic composition difference would lead to σ
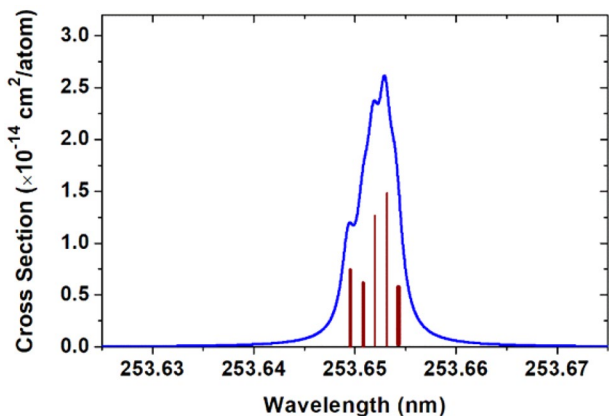
discrepancy between the two channels and, thus, degrade the measurement accuracy correspondingly.

3 Laser output optimizations

3.1 Optimization of laser emission mode by an external cavity

The free-running emission of the employed FP-type green DL contains more than 30 longitudinal modes centering around 505 nm, as shown in Fig. 2. In this work, an external cavity equipped with a 2400 l/mm grating of Littrow type is used to shift the center wavelength of the laser radiation to the required 507.3 nm and concentrate most of the laser power to one mode, as shown in Fig. 2. When operating with this external cavity, the working temperature of the DL is correspondingly raised to 45 °C to make the center of the laser gain curve closer to 507.3 nm and, thus, achieve a required stable laser emission.

3.2 Enhancement of laser output stabilization by PZT dithering

To achieve a faster wavelength modulation and, thus, a better sensitivity, the WMS in this study is performed by modulating the laser injection current rather than the external cavity. As the laser wavelength changes with injection current, the coupling between the laser and the cavity varies, which leads to frequent mode hops and laser intensity oscillations, as shown in Figs. 3a and 4a. To stabilize the laser output, the length of the external cavity is dithered by vibrating the grating at 9 Hz through PZTs. With PZT dithering, the single dominant laser mode with frequent mode hops turns to
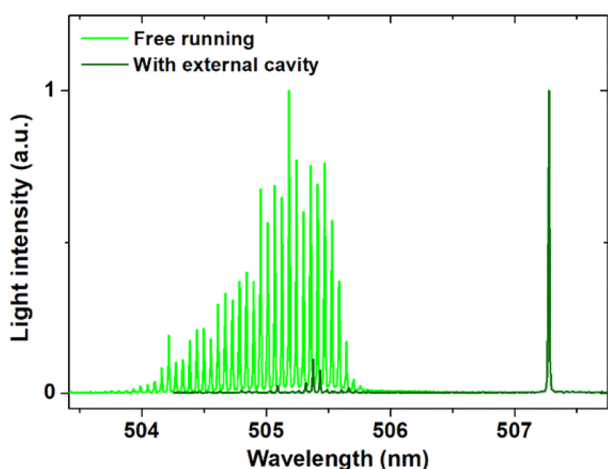

Fig. 2 Measured emission spectra of **a** a free-running green DL operating at 100 mA and 25 °C and **b** an external-cavity equipped DL operating at 100 mA and 45 °C
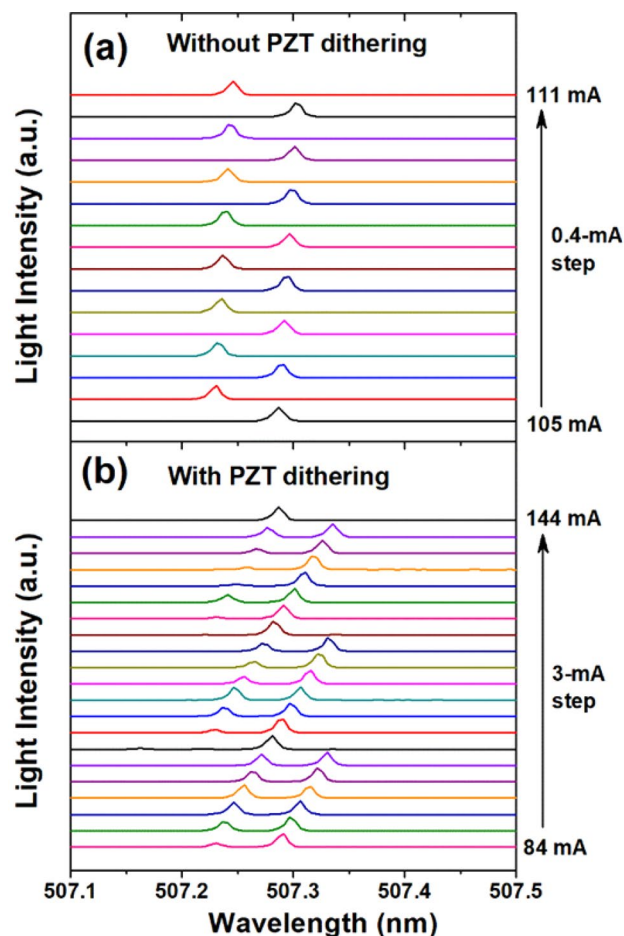

Fig. 3 Measured local emission spectra of the external-cavity equipped DL operating at different currents **a** with a constant cavity length and **b** with the cavity length dithered. The visible peaks indicate the major laser modes

double dominant laser modes but with much better output stability in both laser wavelength and intensity, as shown in Figs. 3b and 4b. The wavelength interval between the two dominant laser modes is around 0.06 nm (~ 70 GHz), which is much larger than the linewidth of the mercury absorption profile (as shown in Fig. 1). Therefore, only one laser mode is absorbed at each time.

4 Experimental setup

Figure 5 shows a schematic diagram of the SHG-WMS experimental setup based on the one employed in our previous mercury sensing works [22]. The changes of the setup mainly lie in the WMS configuration and the solar-blind detection unit used in this work, which are here described in detail, while the other parts of the experimental setup are briefly outlined. The WMS is implemented by superimposing a 20-kHz sinusoidal modulation on the 20-Hz ramping
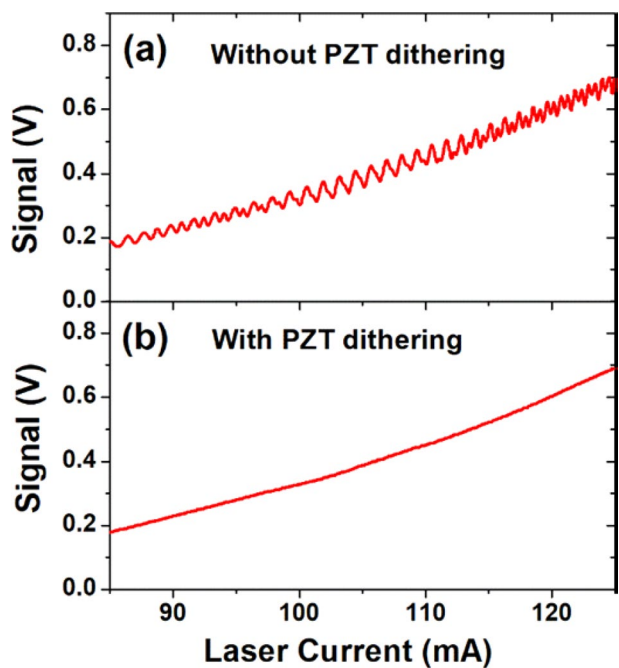
Fig. 4 Measured laser intensity output as the laser current varies **a** with a constant cavity length and **b** with the cavity length dithered
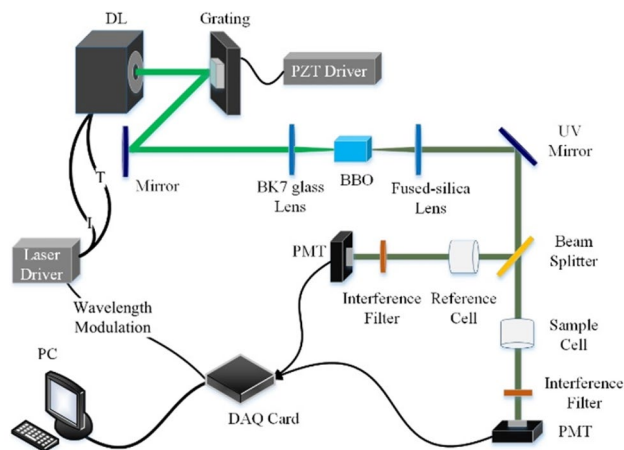

Fig. 5 Diagram of the SHG-WMS system for mercury detection

current of the green DL (Toptica, LD-0505, 80 mW). The sine wave and ramp signals are generated using a multi-function data acquisition (DAQ) card (National Instruments, USB-6356) which is also used for acquisition of the final detected signals. The recorded signals were demodulated by LabVIEW-based lock-in software at 2f of the modulation frequency (40 kHz) with a time constant of 0.1 ms. The UV tunable laser around 253.65 nm is generated through an SHG process using a Beta-Barium-Borate (BBO) nonlinear optical crystal. The UV laser power is measured to be ~ 5 nW according to the radiant sensitivity of the photomultiplier

(PMT, Hamamatsu, H11461). To perform MDL-COSPEC, the laser beam is split into two paths passing through the sample and the reference mercury cells, respectively. In contrast to the previous work, the generated UV laser is not separated from the fundamental green laser; rather, the fundamental visible laser is used as the guiding light, which greatly reduces the system complexity and simplifies the optical-path adjustment. The fundamental laser is efficiently suppressed using UV mirrors, bandpass interference filters, and solar-blind PMTs.

5 Measurement results and analysis

5.1 Optimization of wavelength modulation depth

According to the principle of WMS [17, 29], there exists an optimum modulation depth for each WMS harmonic component to achieve the highest signal amplitude. Although the optimum modulation conditions for common absorption line shapes have been well studied [29], they are hardly adaptable here to the measured absorption signals having irregular line shapes. Therefore, in this work, the optimum modulation amplitude of DL injection current for WMS-2f signals is determined by experiments. Saturated mercury vapor bathing in air at room temperature and near atmospheric pressure inside a cell of 2.253-mm length is measured. Figure 6 shows the acquired WMS-2f peak amplitude as a function of modulation current amplitude, from which the optimum modulation amplitude is determined to be 20 mA. As can also be seen in Fig. 6, the WMS-2f signal amplitude changes slowly in the vicinity of the maximum value. Therefore, although the absorption line shape may slightly change during the measurement due to laser-mode competitions, the optimum modulation parameter would still be applicable for
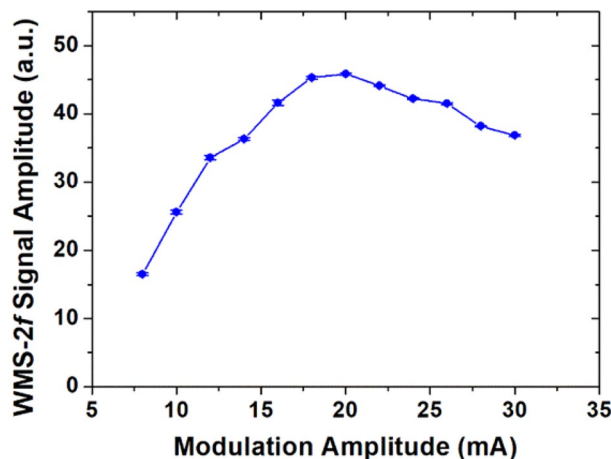

Fig. 6 Plot of the measured WMS-2f peak amplitude as a function of the current modulation amplitude

achieving a high signal amplitude. Note that since the line shape change in the sample and the reference channel is identical, laser-mode competitions have negligible effect on the measurement results.

5.2 WMS-2*f* signal measurement

To perform WMS-2*f* signal measurement, both the sample and the reference gas cells are filled with saturated mercury vapor bathing in air at room temperature and near atmospheric pressure. During the measurement, the room temperature is measured to be 24.7 ± 0.3 °C with the corresponding mercury saturation concentration of 20.6 ± 0.5 mg/m^3. The mass concentration of the saturated mercury vapor is calculated using the mercury vapor pressure correlation given by Huber et al. [34]. We note that, by the commonly used Dumarey equation [35], the calculated mercury concentration would be slightly lower (~5%). By comparison, according to recent studies, the mercury vapor pressure correlation published by Huber et al. is more accurate to predict the mass concentration of saturated mercury vapor in air [24, 36]. However, this discrepancy has negligible effect on the measurement, because the sample and the reference cell are at the same room temperature and have an identical mercury mass concentration. The lengths of the used sample and reference cells filled with saturated mercury vapor are 1.056 mm and 3.261 mm, yielding pathlength-integrated mercury concentrations of 21.8 ± 0.5 μg/m^2 and 67.2 ± 1.6 μg/m^2, respectively. Since the typical mercury concentration in the ambient air is as low as 2 ng/m^3 [37], it has negligible effect on the measurement.

Figure 7a shows an example of the acquired raw WMS-2*f* signal pair with an integration time of 10 s (200 scans averaged). The corresponding DAS signal can be referred to [27]. It can be clearly seen that the original WMS-2*f* signals are seriously disturbed by large backgrounds mainly coming from residual amplitude modulation and etalon fringes. The SHG output intensity generally presents a complex nonlinear behavior because of its quadratic dependence on the fundamental light intensity as well as dependence on the phase-matching condition changing with wavelength scan. Consequently, in an SHG-WMS system, there always exist relatively large RAM background signals [38, 39]. To reduce the background interference, in this study, the background signals are separately acquired using gas cells filled with only air (i.e., mercury absorption free) and then subtracted from the original signals. Figure 7b presents the WMS-2*f* signal pair after background correction, showing that the large background signals are effectively removed. Compared with DAS, the WMS significantly reduces the difficulty in the extraction of small mercury absorption signals from the large and complex SHG light background, delivering robust measurement results. For retrieval of the sample mercury
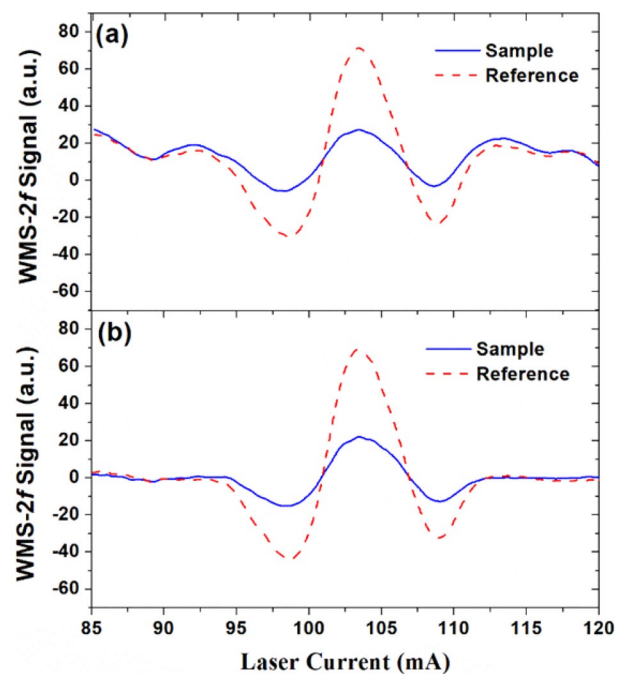

Fig. 7 Example of the measured WMS-2*f* signal pairs with 200 scans averaged. **a** Raw signals; **b** signals with background correction. The path length-integrated mercury concentrations of the sample and the reference cells are determined to be 21.8 ± 0.5 μg/m^2 and 67.2 ± 1.6 μg/m^2, respectively

concentration, the magnitude ratio between the WMS-2*f* signals is calculated by fitting the sample signal to the reference signal employing a multiple-linear-regression fitting approach, which is detailed in [26].

5.3 Performance evaluation

For quantitative mercury sensing, measurement sensitivity and linearity are two of the most important capabilities and are here evaluated. The sensitivity of the proposed SHG-WMS mercury sensing system is evaluated by performing Allan–Werle variance analysis [40]. The sample and the reference mercury cells are those used in Sect. 5.2. The concentration of the sample cell is retrieved according to Eq. (4). Figure 8a shows the plots of successively acquired 1-s data (averaged over 1 s) in 1 h. The corresponding Allan–Werle deviation (square root of the Allan–Werle variance) plots are shown in Fig. 8b, indicating a sensitivity of 0.15 μg/m^3 for 1-m pathlength with an integration time of 10 s. Although only part of the whole laser power is utilized in WMS-2*f* measurement, an improved sensitivity is still achieved, which is 25% better than the one obtained in our previous work using the DAS scheme [22].

To evaluate the measurement linearity, 11 different path-length-integrated concentrations of mercury obtained using mercury-saturated cells with various lengths are measured.
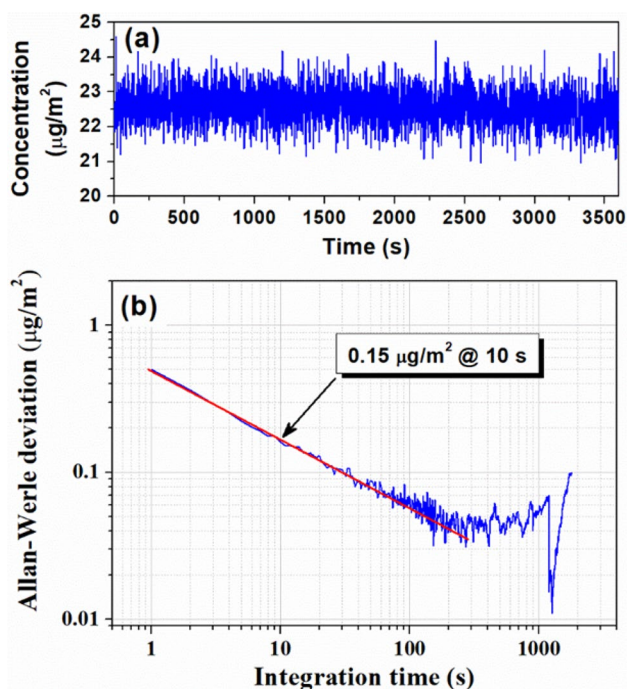
Fig. 8 **a** Plots of successively measured 1-s data of mercury concentration in 1 h and **b** the corresponding Allan–Werle deviation plots

Figure 9 shows scatter plot of the measured results against calculated values. Each measured concentration is an average of 20 repeatedly measured values with each taking 10 s. Linear regression is carried out on data under 60 μg/m². The coefficient of determination of the linear fit $R^2 = 0.9995$, and the standard deviation of the fit residuals is only 0.51 μg/m², which indicate that, within the range of 60 μg/m², the system has a highly linear response. The linear response range and the linearity level of the proposed SHG-WMS system are
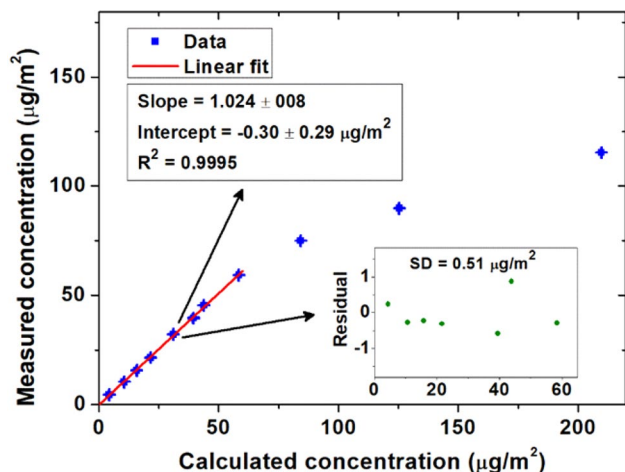
comparable with those obtained by the SHG-DAS scheme [22]. For detection of high-concentration mercury, a pre-determined calibration curve can be used to guarantee the measurement accuracy.

6 Discussion on sensitivity improvement

6.1 Performance limit of sensitivity

To evaluate the advantage of WMS and analyze the factors limiting the system sensitivity, the relative intensity noise (RIN) of the laser source is measured. The RIN is defined in a 1-Hz bandwidth as follows [41]:

$$\mathrm{RIN}(f) = \frac{S_{\delta P}(f)}{P_0^2}, \tag{5}$$

where $S_{\delta P}(f)$ is the intensity noise power spectral density and P_0 is the average optical power. The RIN measurement is performed by measuring the noise spectrum of the recorded PMT signal with the laser operating at a constant current of 100 mA. The PMT signal is acquired at a sample rate of 1 MS/s over 5 s. Figure 10 shows the measured RIN with a resolution of 20 Hz for laser with and without external-cavity dithering, as well as the noise floor when the laser is turned off. As can be clearly seen, without laser cavity dithering, the noise level almost becomes flat beyond 500 Hz (the roll off around 50 kHz is mainly due to the detector bandwidth limitation). This flat noise level corresponds to the shot-noise-limit. In general, shot noise is transformed to photocurrent variance described by $2qI_{\mathrm{ave}}B$, where q is the electronic charge, I_{ave} is the average photocurrent corresponding to the average optical power, and B is the detection

Fig. 9 Scatter plot of the measured mercury concentration against the calculated values. The inset shows the residual of linear fit
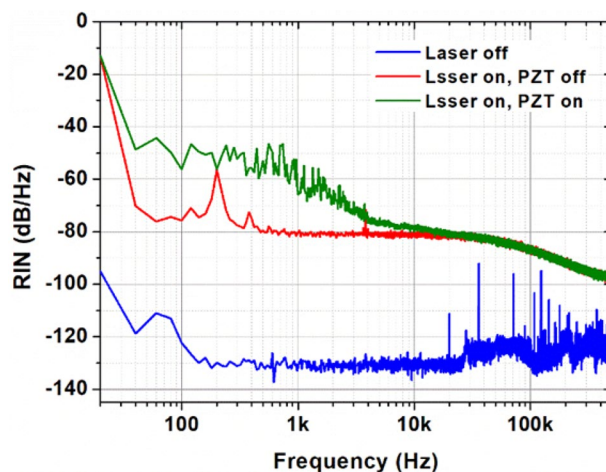

Fig. 10 Measured RIN for laser with and without external cavity dithering and the thermal noise floor (when the laser is turned off)

bandwidth. Then, according to Eq. (5), the shot-noise-limited RIN, which is independent on frequency, can be given by the following:

$$RIN_{sh} = 10 \log_{10} 2qB/I_{ave}. \qquad (6)$$

According to the recorded signal voltage of 0.3 V, load resistance of 10 kΩ, and PMT current gain of 2.3×10^6, I_{ave} is estimated to be 1.3×10^{-11} A. Then, the 1-Hz-bandwidth RIN_{sh} is calculated to be -76 dB/Hz, which is basically consistent with the flat noise level of -81 dB/Hz, as shown in Fig. 10. The 5-dB difference is mainly attributed to the uncertainty of the PMT current gain.

At the shot-noise-limit condition, implementation of WMS with high modulation frequency would not bring any benefit to the measurement sensitivity. On the other hand, when the cavity is dithered (the necessity of cavity dithering is detailed in Sect. 3), much low-frequency flicker noise is generated which is more than 20 dB (10 times) higher than the shot noise beyond 10 kHz. In such situation, considering that the signal amplitude of WMS-2f is about 0.3 times that of direct absorption [42], an improvement in signal-to-noise ratio (SNR) by a factor of 3 can be expected. However, the detection bandwidth of the WMS system is about ten times higher than that of previous DAS system (8 Hz vs. 0.75 Hz), which cancels out the increase in SNR. Consequently, only a slight improvement in the sensitivity is achieved by the current SHG-WMS scheme. Thus, to obtain a larger sensitivity improvement, a straightforward way is reducing the shot noise level using a laser with high power.

6.2 Performance improvement by higher harmonic WMS

As mentioned above, the amplitude of RAM background in an SHG-WMS system is particularly high. Although the large background noise can be efficiently suppressed through subtraction, it is not adaptable to in-site mercury monitoring where a reference zero gas is not available, In Refs.[38, 39], Kluczynski et al. comprehensively investigated the background signals in an SHG-WMS system, and found that the RAM background signals for 4f- and 6f-detections were considerably lower than those for 2f detection. This implies that a better sensitivity can be achieved by detecting higher harmonic WMS components even without background correction. Figure 11 shows 2f, 4f, and 6f WMS signals of mercury with the same modulation current of 20 mA. The 2f signal has a much larger background than those of 4f and 6f signals, which is consistent with the conclusion in Refs. [38, 39].

To examine the capability of higher-harmonic WMS for sensitivity improvement, we measure the background signal amplitudes and thus obtain the signal-to-background ratios (SBRs) for 2f, 4f, and 6f harmonic components as a function of the modulation amplitude, which are shown in

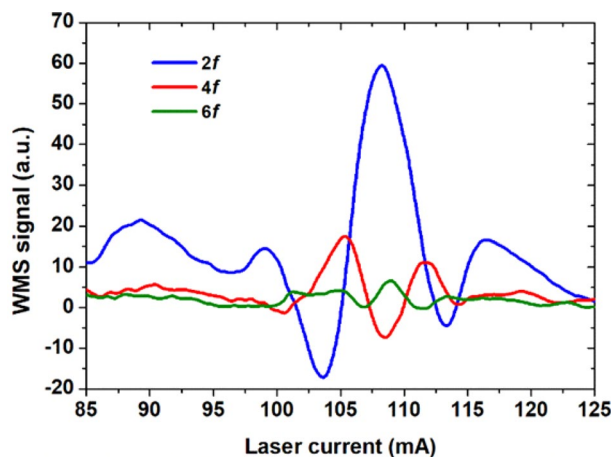**Fig. 11** 2f, 4f, and 6f WMS signals of mercury with a modulation amplitude of 20 mA

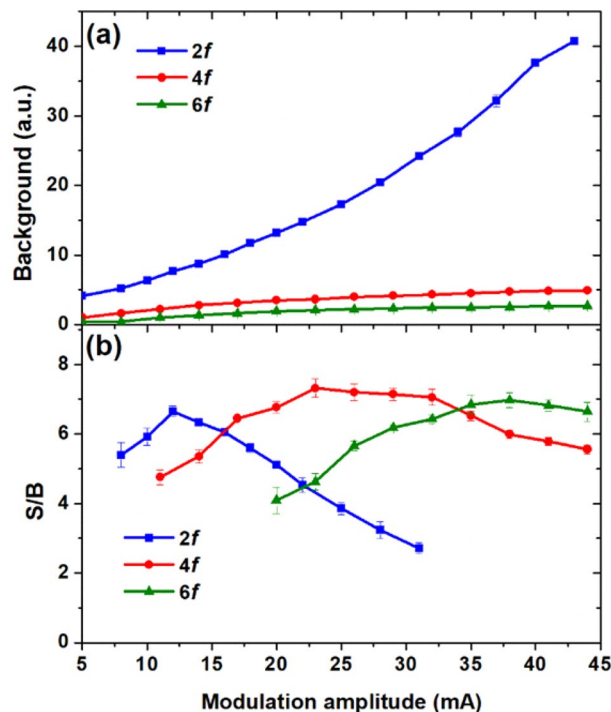**Fig. 12** Plots of **a** background amplitude and **b** signal-to-background ratio for 2f, 4f, and 6f WMS signals versus the modulation amplitude

Fig. 12. The background signal amplitude is measured as the average of the absolute values of the mercury-absorption-free WMS signals within a ramp scan. The amplitude of the WMS signal is measured as its peak-to-peak value. Despite the considerable background reduction for 4f and 6f harmonic components, the maximum SBRs achieved are slightly larger than that obtained by 2f detection. This unexpected result can be attributed to the severe etalon effects in the SHG-WMS system [38, 39]. Thus, to take advantage

of the low-level RAM background of the higher harmonic WMS, relatively large interference fringes should be effectively suppressed in advance by special techniques such as Brewster-plate spoilers [43, 44].

7 Conclusion

We have, for the first time, demonstrated an SHG-WMS-based mercury sensing method. Compared with our previous SHG-DAS work [22], the main achievements in the current SHG-WMS work can be concluded in three aspects:

(1) After careful characterization of the laser outputs of intensity and spectrum, the SHG-WMS mercury sensing system is established and optimized, achieving a better sensitivity while maintaining a comparably high linearity. By scrutinizing the relative intensity noise (RIN) of the laser source, the sensitivity limitation of the current SHG-WMS system is determined to be the shot noise, which can be efficiently dealt with using a high-power laser. (2) Compared with DAS, the WMS significantly simplify the extraction of small mercury absorption signals from the large and complex SHG light background, making the measurement robust and efficient. (3) For practical in-site mercury monitoring applications, high-harmonic ($4f$ and $6f$) detections are performed, showing a great potential for suppression of the large RAM background always existing in an SHG-WMS system.

In the near future, when high-power DFB-type green diode lasers are commercially available, the SHG-WMS-based method would be highly competitive in mercury sensing applications. In addition, other sensitive techniques can be exploited to further improve the measurement SNR, e.g., increasing the absorption pathlength using multipass cells [45]. Therefore, although the improvement of sensitivity in this work is slight (only 25% compared to the previous SHG-DAS system), the results of this work would be valuable and constructive for the design of a high-performance SHG-WMS-based mercury sensing system for the future.

References

1. UNEP, Global Mercury Assessment 2013: Sources, emissions, releases and environmental transport (UNEP Chemicals Branch, Geneva, Switzerland) (2013).
2. UNEP, Minamata convention on mercury (UNEP, Geneva, Switzerland) (2013)
3. J.H. Pavlish, E.A. Sondreal, M.D. Mann, E.S. Olson, K.C. Galbreath, D.L. Laudal, S.A. Benson, Fuel. Process. Technol. **82**, 89 (2003)
4. R.J. Valente, C. Shea, K.L. Humes, R.L. Tanner, Atmos. Environ. **41**, 1861 (2007)
5. L. N. Suvarapu and S. O. Baek, Int. J. Anal. Chem. **2017**, 3624015 (2017).
6. D.L. Laudal, J.S. Thompson, J.H. Pavlish, L.A. Brickett, P. Chu, Fuel. Process. Technol. **85**, 501 (2004)
7. P.C. Swartzendruber, D.A. Jaffe, B. Finley, Atmos. Environ. **43**, 3648 (2009)
8. A.A. El-Feky, W. El-Azab, M.A. Ebiad, M.B. Masod, S. Faramawy, J. Nat. Gas. Sci. Eng. **54**, 189 (2018)
9. K.H. Kim, V.K. Mishra, S. Hong, Atmos. Environ. **40**, 3281 (2006)
10. S.B. Darby, P.D. Smith, D.S. Venables, Analyst **137**, 2318 (2012)
11. A. Pierce, D. Obrist, H. Moosmuller, X. Fain, C. Moore, Atmos. Meas. Tech. **6**, 1477 (2013)
12. A.M. Pierce, C.W. Moore, G. Wohlfahrt, L. Hortnagl, N. Kljun, D. Obrist, Environ. Sci. Technol. **49**, 1559 (2015)
13. M. Lian, L.H. Shang, Z. Duan, Y.Y. Li, G.Y. Zhao, S.M. Zhu, G.L. Qiu, B. Meng, J. Sommar, X.B. Feng, S. Svanberg, Environ. Pollut **240**, 353 (2018)
14. L. Mei, G.Y. Zhao, S. Svanberg, Opt. Lasers Eng. **55**, 128 (2014)
15. D. Bauer, S. Everhart, J. Remeika, C.T. Ernest, A.J. Hynes, Atmos. Meas. Tech. **7**, 4251 (2014)
16. J. Hodgkinson, R.P. Tatam, Meas. Sci. Technol. **24**, 012004 (2013)
17. P. Werle, Spectrochim. Acta A **54**, 197 (1998)
18. J. Alnis, U. Gustafsson, G. Somesfalean, S. Svanberg, Appl. Phys. Lett. **76**, 1234 (2000)
19. A.E. Carruthers, T.K. Lake, A. Shah, J.W. Allen, W. Sibbett, K. Dholakia, Opt. Commun. **255**, 261 (2005)
20. T.N. Anderson, J.K. Magnuson, R.P. Lucht, Appl. Phys. B **87**, 341 (2007)
21. G. Almog, M. Scholz, W. Weber, P. Leisching, W. Kaenders, T. Udem, Rev. Sci. Instrum. **86**, 033110 (2015)
22. X.T. Lou, T. Zhang, H.Z. Lin, S.Y. Gao, L.J. Xu, J.N. Wang, L. Wan, S.L. He, Opt. Express **24**, 27509 (2016)
23. J. Paul, Y. Kaneda, T.L. Wang, C. Lytle, J.V. Moloney, R.J. Jones, Opt. Lett. **36**, 61 (2011)
24. A. Srivastava, J.T. Hodges, Anal. Chem. **90**, 6781 (2018)
25. X.T. Lou, G. Somesfalean, B. Chen, Y.G. Zhang, H.S. Wang, Z.G. Zhang, S.H. Wu, Y.K. Qin, Opt. Lett. **35**, 1749 (2010)
26. X.T. Lou, G. Somesfalean, Z.G. Zhang, Appl. Opt. **47**, 2392 (2008)
27. X.T. Lou, G. Somesfalean, S. Svanberg, Z.G. Zhang, S.H. Wu, Opt. Express **20**, 4927 (2012)
28. Y. Arita, P. Ewart, Opt. Commun. **281**, 2561 (2008)
29. P. Kluczynski, J. Gustafsson, A. Lindberg, O. Axner, Spectrochim. Acta B **56**, 1277 (2001)
30. https://physics.nist.gov/PhysRefData/Handbook/Tables/mercurytable1.htm
31. W.G. Schweitzer Jr., J. Opt. Soc. Am. **53**, 1055 (1963)
32. F. Bitter, Appl. Opt. **1**, 1 (1962)
33. R.Y. Sun, J.E. Sonke, L.E. Heimburger, H.E. Belkin, G.J. Liu, D. Shome, E. Cukrowska, C. Liousse, O.S. Pokrovsky, D.G. Streets, Environ. Sci. Technol. **48**, 7660 (2014)
34. M.L. Huber, A. Laesecke, D.G. Friend, Ind. Eng. Chem. Res. **45**, 7351 (2006)
35. R. Dumarey, R.J.C. Brown, W.T. Corns, A.S. Brown, P.B. Stockwell, Accredit. Qual. Assur. **15**, 409 (2010)
36. C.R. Quétel, M. Zampella, R.J.C. Brown, Trac-Trend. Anal. Chem. **85**, 81 (2016)
37. K.H. Kim, R. Ebinghaus, W.H. Schroeder, P. Blanchard, H.H. Kock, A. Steffen, F.A. Froude, M.Y. Kim, S.M. Hong, J.H. Kim, J. Atmos. Chem. **50**, 1 (2005)

38. P. Kluczynski, A.M. Lindberg, O. Axner, Appl. Opt. **40**, 783 (2001)
39. P. Kluczynski, A.M. Lindberg, O. Axner, Appl. Opt. **40**, 794 (2001)
40. P. Werle, Appl. Phys. B **102**, 313 (2011)
41. C. Thibon, F. Dross, A. Marceaux, N. Vodjdani, IEEE Photonic Tech. Lett. **17**, 1283 (2005)
42. O. Axner, P. Kluczynski, A.M. Lindberg, J. Quant. Spectrosc. Radiat. Transf. **68**, 299 (2001)
43. C.R. Webster, J. Opt. Soc. Am. B **2**, 1464 (1985)
44. C.R. Markus, A.J. Perry, J.N. Hodges, B.J. McCall, Opt. Express **25**, 3709 (2017)
45. X.T. Lou, C. Chen, Y.B. Feng, Y.K. Dong, Opt. Lett. **43**, 2872 (2018)